Chapter 6

$La_{1-x}K_xFeO_{3-\delta}$: An anion intercalative pseudo-capacitive electrode for supercapacitors application

6.1 Introduction

To move away from fossil fuel-based energy solutions and to produce power and electricity through renewable energy generated through sources like solar, wind, and tidal energy large-scale electrochemical energy storage system is required.[1-2] Electrochemical energy storage devices such as batteries and electrochemical capacitors are empowering potable electronics and broad range electricity transmission through grid regulation and the transport sector.[3] An electrochemical cell is generally made of two electrodes separated by an electrolyte (a high ionic conductor made of aqueous and non-aqueous materials). As per the charge storage mechanism, electrochemical energy storage (EES) system are classified into three categories: a) electric-double layer capacitors (EDLCs); which contains carbon-based material due to its high conductivity and high surface area available to adsorb electrolyte ions onto surfaces to form electric double layer charge storage through electrified material [4-5], b) battery; it stores electrical energy as chemical energy in two electrodes, a reductant (anode) and an oxidant (cathode), separated by an electrolyte that allows transport of the ionic composition of the chemical reaction to be stored inside the electrode materials.[6] c) pseudo capacitors, in addition to an electrostatic electric double layer, it stores electrical energy in a faradaic component resulting normally from a shallow insertion of the mobile ions of electrolyte into an electrode host with the reduction of a host-electrode cation.[7] E vs t plot behaviour for EDLC (surface charge storage) is linear and for battery (faradic reaction); it is nonlinear and for pseudocapacitor (combination of faradic and surface charge storage); it is more linear compared to battery.[8-9] RuO_2 was the first extensively studied material to show pseudocapacitance behaviour and continue to be an excellent capacitance material due to its high chemical stability and conductivity.[10] However, its scarcity and high cost

limit its application for commercial purposes, and as an alternate MnO_2 was demonstrated to posse pseudocapacitive behaviour.[11] Vigorous studies started on transition metal oxide-based materials such as NiO, V_2O_5, spinel Co_3O_4, Fe_2O_3, and mixed spinel $NiCo_2O_4$ to explore as an electrode of pseudocapacitor.[12-18] Perovskite type $LaMnO_3$ was demonstrated as an anion-intercalation pseudocapacitor.[19] Perovskite oxides have the unit cell formula ABO_3 where the A-site is either alkaline or lanthanide element while the B-site is a transition metal element. By strategically selecting the A-site elemental composition, one can readily control the B-site element's oxidation state as well as the overall oxygen vacancy content via charge compensation.[20-21] Perovskite supercapacitors have attracted widespread attention and several perovskites such as $LaNiO_3$[22], $LaFeO_3$[23], $La_xSr_{1-x}NiO_{3-\delta}$[23], $La_xSr_{1-x}CoO_{3-\delta}$[24], $La_xSr_{1-x}Cu_{0.1}Mn_{0.9}O_{3-\delta}$ [25], $Sr_2CoMoO_{6-\delta}$ [26], $La_{0.85}Sr_{0.15}MnO_3$ [27] were investigated for pseudo-capacitance applications.

Perovskites are a very important class of electronic materials, especially layered perovskites such as $YBa_2Cu_3O_7$ [28], $La_2CuO_{4.032}$ [29], $LaCsNb_2O_7$ [30], and $LaKNb_2O_7$ [30]. YBa2Cu3O7 crystallizes in orthorhombic perovskite structure where an alternate layer of Y and Ba induced an inter-planer potential that generates cooper–pairs and stabilized Cu^{3+} ion in the B site octahedral responsible for high-temperature Superconducting properties of the materials. The effect of the internal field was also presented in the layered perovskite Na*Ln*TiO4 (Ln = Y, La-Tb), where the internal potential generated over Ti octahedral, generated the systematic shift in the redox energy of $Ti^{4+/3+}$ couples.[31] Similarly, here, I envisaged the concept of accessing higher redox energies through the incorporation of internal layer potential to achieve multiple electron transfers such as $Fe^{4+} \rightarrow Fe^{2+}$ for higher pseudocapacitive energy storage. In this chapter, I have investigated the concept of layered potential on transitional metal-ion octahedral to utilize high redox energies (higher oxidation state such as $Fe^{4+/2+}$) for the fabrication of high-capacity electrodes. Using La/K ordering in orthorhombic perovskite; $La_{1-x}K_xFeO_{3-\delta}$, Fe^{4+} oxidation state is accessed, and a systematic shift in redox energy ($Fe^{4+/3+}$ and $Fe^{3+/2+}$) with K^+ ion doping on A site of $LaFeO_3$ perovskite is shown and in turn, high pseudo-capacitance of the electrode is demonstrated. A specific capacitance of 662F/g equivalent to 1.32 e-/mole charge transfer was observed for $La_{0.5}K_{0.5}FeO_{3-\delta}$ in an aqueous 2M KOH electrolyte in a voltage window of 1V. The detailed synthesis, characterizations, and electrochemical performance of $La_{1-x}K_xFeO_{3-\delta}$ are presented

6.2 Materials Synthesis and characterizations

The solid-state ceramic synthesis route was utilized to synthesize crystalline K-doped $La_{1-x}K_xFeO_{3-\delta}$ ($0 \leq x \leq 0.5$), because the solid-state synthesis route in general produces more thermodynamically stable compounds. La_2O_3 (99.9%), K_2CO_3 (99.9%), and Fe_2O_3 (99.9%) were taken as a precursor for the synthesis of materials. The precursors are taken in stoichiometric ratio and mixed in agate mortar-pestle for about 30 minutes. The mixture is then fired in a platinum crucible at 1050^{o}C for 12 hours for the preparation of $LaFeO_3$ and at 1150^{o}C for 12 hours for the preparation of $La_{1-x}K_xFeO_{3-\delta}$ ($0 \leq x \leq 0.5$), followed by slow cooling to room temperature. Multiple heating and grinding of the samples were carried out to get single-phase materials. The phase formation was studied through Rigaku Miniflex desktop X-ray Diffractometer (XRD) with Cu-Kα radiation (λ = 1.54 Å) in the range $2\theta \sim 20 - 90°$ with a step size of 0.02°. The structures were refined by the Rietveld refinement method using FULLPROF suite software and orthorhombic perovskite (Pnma, space group 62) was taken as the model structure. The microstructures of the sintered samples were investigated by using a scanning electron microscope (EVO - Scanning Electron Microscope MA15/18). The average grain size was calculated using the linear intercept method with ImageJ software. Pore size distribution and specific surface area of the sample were measured by BET (MicrotracBEL).

X-ray Photo-electron Spectroscopy (XPS) studies were carried out to investigate the electronic structures of the materials. XPS of the sample was carried out by Thermo Scientific Multilab 2000 instrument using Al Kα radiation operated at 150W. Binding energies reported here are concerning C (1s) at 284.5 eV and they are accurate within ±0.1 eV. The oxidation state of Fe and oxygen stoichiometry was determined by chemical analysis using a redox titration method called iodometry. 20mg of active materials were dissolved in 30ml hydrochloric acid (3M) in the presence of 24mg potassium iodide (KI), and the liberated iodine was titrated with sodium thiosulfate $Na_2S_2O_3$ (1M) using starch as an indicator. Concordant results for oxygen stoichiometry were obtained within an error of ±0.01. High purity Argon gas was a bubble in the solution to avoid oxygen contamination from air and double-distilled preheated water was used in titration to avoid any dissolved oxygen contamination and active bacteria present in the water.

6.2.1 Electrochemical Studies:

The electrochemical measurements were carried out using nova 2.0 autolab. The catalyst ink was prepared by homogenizing 35 mg of catalyst, 10 mg of acetylene black, and 5 mg PVDF binder in 1 mL of NMP solvent under an ultrasonication bath for 40 min. To investigate the activity of the supercapacitance, an aliquot of 20 μL of homogenized ink was deposited by a micropipette onto the surface of a carbon paper (Torrey carbon paper, alfa Aesar) (1cm*1cm area) and dried under an IR lamp. The electrode loading was calculated by taking the weight of the electrode through electronic balance (error limit: 0.01mg). For that, the first weight of Torrey paper was taken then the weight of coated electrode (after drying the coated ink on Torrey carbon paper on a 1x1cm^2 area was taken for the study. Then from the difference in the weight exact loading of electrode material was calculated. The total material load was typically 1 mg (0.7mg active material: carbon: PVDF binder).

Cyclic voltammetry (CV), galvanometric charge/discharge, and electrochemical impedance spectroscopy (EIS) in a conventional three-electrode arrangement were used to determine the electrochemical characteristics of the prepared pseudocapacitor measurement was done by Metrohm Autolab (PGSTAT204) equipped with FRA32M module. Electrochemical measurements were analyzed using NOVA 2.0 software.

Pt was used as a counter-electrode and Hg/HgO (1M KOH) was utilized as a reference electrode. All electrodes were measured in 2M KOH electrolyte, cyclic voltammetry (CV) was used to show redox behavior, Chronopotentiometry was used for charge-discharge capacity measurements and EIS was employed for overall internal resistance measurements.

6.3 Results and Discussions:

6.3.1 Crystallographic characterization

XRD pattern of prepared materials treated at 1150^o C for 12 hours is shown in **Figure 6.1(.a)** for $La_{1-x}K_xFeO_{3-\delta}$ ($0 \leq x \leq 0.5$), All the synthesized materials show a single-phase formation. The prominent single-phase diffraction peak matches well with the JCPDS file: 1526450. Structure parameters derived from Rietveld refinement show that the (002) peak (highest intensity peak) shifted linearly to a lower 2θ value with increasing dopant (K) concentration on the La site. As ionic radii of K^+ (1.64Å, 12

coordination) is greater than La^{3+} (1.36Å, 12 coordination), [32] doping of K on La site will result in peak shifting to a lower 2θ value.

Rietveld refined XRD profile of $La_{0.5}K_{0.5}FeO_{3-\delta}$ is provide in **Figure 6.1(b)**. Rietveld refinement studies **of** $La_{1-x}K_xFeO_{3-\delta}$ ($0 \leq x \leq 0.5$), show that all materials adopted orthorhombic (Pnma, space group 62) type structure. In the orthorhombic cell, large percentages of La^{3+} ions were replaced by K^+ ions, this may result in a formation of La and K alternating layers as shown in **Figure 6.1(c).**

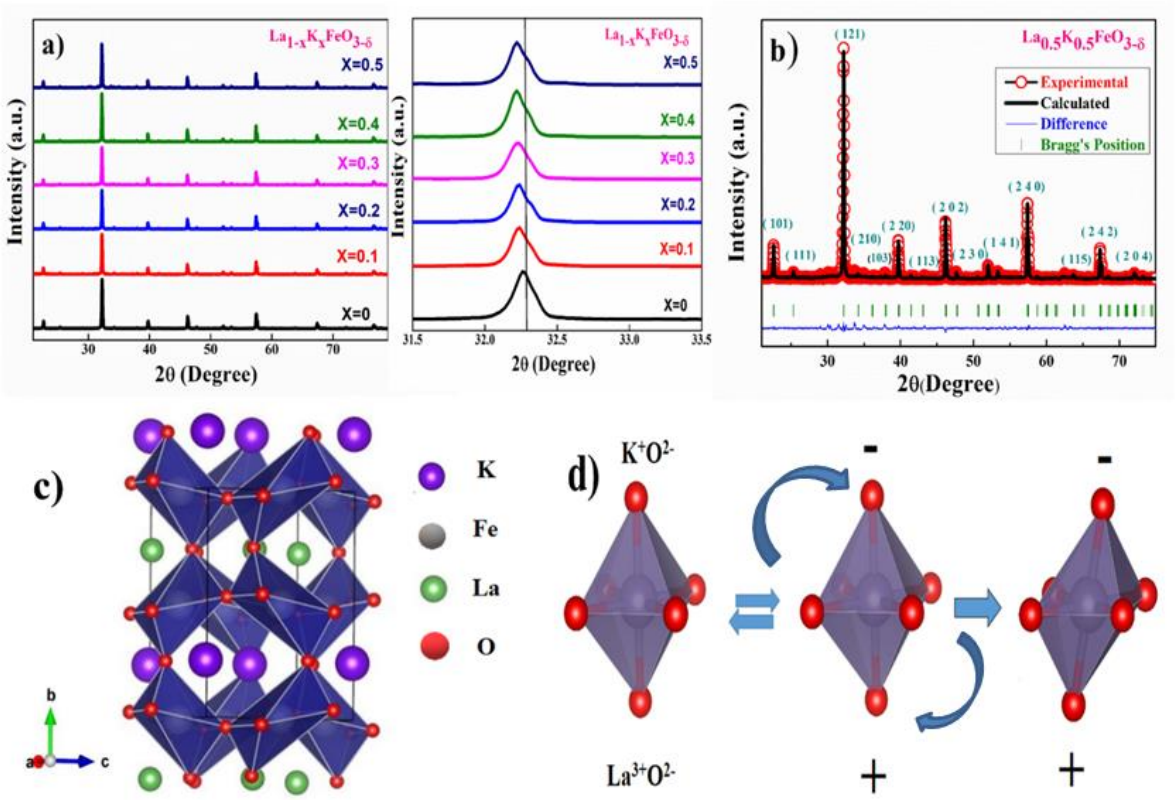

Figure 6. 1. (a) XRD pattern of $La_{1-x}K_xFeO_{3-\delta}$ ($0 \leq x \leq 0.5$), (b) Rietveld refinement of $La._5K._5FeO_{3-\delta}$, (c) structure of $La._5K._5FeO_{3-\delta}$ and (d) Jahn–Teller distortion over Fe-O octahedra in orthorhombic $La._5K._5FeO_{3-\delta}$ structure.

The alternating layer of La and K can be built a charge potential over Fe-O octahedra, resulting in tilt in bond angle and elongation in non-planer bonding resulting in a Jahn-Teller type structural distortion of Fe-O octahedral as shown in **Figure 6.1(d)** (vista image). This distortion favors the in-situ formation of Fe^{4+} (electronic configuration: $t_{2g}^3e_g^1$) to support the Jahn-Teller distortion. Thus this internal potential effects or shifts the redox energy of Fe in such a way that $Fe^{4+/3+}$ and $Fe^{3+/2+}$

redox couples can become accessible to facilitate superior pseudo-capacitive storage capacity of the materials.

Table 6.1 Structural parameter of $La_{1-x}K_xFeO_3$ ($0 \leq x \leq 0.5$) obtained Rietveld refinement using FULLPROF suite software

Sample	a(A^0)	b(A^0)	c(A^0)	α=β =γ (^{0})	Chi^2	R_{bragg}	R_f	R_{wp}
$LaFeO_3$	5.5638(3)	7.8537(4)	5.5546(3)	90	1.6	1.48	2.59	8.44
$La_{0.9}K_{0.1}FeO_{3-\delta}$	5.5625(2)	7.8481(3)	5.5541(4)	90	2.9	2.94	4.46	12.9
$La_{0.8}K_{0.2}FeO_{3-\delta}$	5.5615(3)	7.8516(3)	5.5533(4)	90	3.72	8.55	13.6	13.7
$La_{0.7}K_{0.3}FeO_{3-\delta}$	5.5596(4)	7.8490(4)	5.5523(3)	90	3.32	5.46	6.43	14.1
$La_{0.6}K_{0.4}FeO_{3-\delta}$	5.5613(5)	7.8515(3)	5.5539(5)	90	4.25	5.17	7.85	13.5
$La_{0.5}K_{0.5}FeO_{3-\delta}$	5.5614(4)	7.8518(5)	5.5549(4)	90	4.33	4.48	7.62	13.6

6.3.2 X-ray photoelectron spectroscopy (XPS) analysis

Survey spectra of $La_{0.5}K_{0.5}FeO_{3-\delta}$ sample containing (C1s), O(1s), Fe(2p), La(3d), K(2s) (377.41eV) and K(2p) (293.16eV) [33a] is shown in **Figure 6.2.(a)** To investigate the Fe oxidation state, XPS of core level Fe(2p) spectra of $La_{0.5}K_{0.5}FeO_{3-\delta}$ and $LaFeO_3$ sample is shown in **Figure 6. 2 (b)** XPS curve is fitted or deconvoluted with the help of XPSPEAK41 software. The peak position indicates that only the Fe^{3+} state is present in $LaFeO_3$ and both $Fe^{3+}$and Fe^{4+} states are present in $La_{0.5}K_{0.5}FeO_{3-\delta}$. For Fe^{3+} oxidation state, binding energies were obtained at 709.95eV (2p3/2) and 723.74eV (2p1/2) and for Fe^{4+} oxidation state, binding energies were obtained at 712.65 eV(2p3/2) , 726.2 eV (2p1/2) with presence of weak satellite peak at 718.40eV. [34] Fe (2p 3/2, 1/2) spectra depict the presence of Fe^{4+} ion as the majority phase in $La_{0.5}K_{0.5}FeO_{3-\delta}$. Fe^{4+} and Fe^{3+} ions ratio were calculated from their peak strength and Fe^{4+} and Fe^{3+} ions were found in the ratio of 85:15 in the materials. **Figure 6. 2. (c) shows** O(1s) spectra of $La_{0.5}K_{0.5}FeO_{3-\delta}$ sample containing two binding energies respectively at O1s(I) (531.16eV) and O1s(II) (529.27eV) due to bonding with two distinctive Fe^{4+} and Fe^{3+} ions present in the materials.(O1s(I) and O1s(II) corresponding lattice and absorbed oxgygen)[33b] **Figure 6. 2. (d)** shows

La(3d) spectra presenting two sets of La(3d)5/2 and La(3d)1/2 peaks at (833.75eV and 850.77eV) (837.49eV and 854.51eV) respectively due to its bonding with two different type of Fe-O octahedral. **Figure 6.2. (e)** shows K(2p) 3/2, 1/2 spectra, at 293.59eV and 295.36 eV respectively .

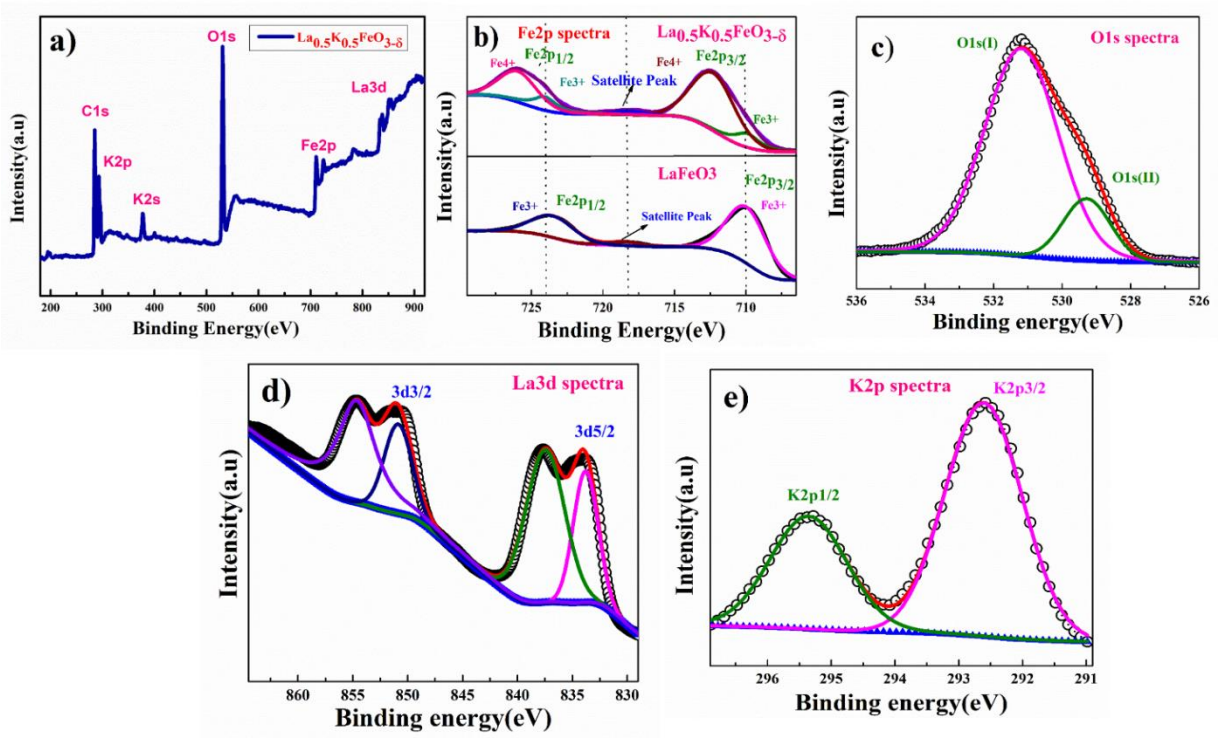

Figure 6. 2. XPS of $La_{0.5}K_{0.5}FeO_{3-\delta}$ of powder sample (a) full survey, (b) Fe(2p) core level, (c) O(1s), (d) La (3d) and (e) K(2p)

Iodomatry titrations were carried out to know the oxygen stoichiometry of the $La_{0.5}K_{0.5}FeO_{3-\delta}$ sample, and oxygen content was found close to 2.92±0.01. This suggests that $La_{0.5}K_{0.5}FeO_{2.92}$ sample contains 84% Fe^{4+} and 16% of Fe^{3+}. This study matches very well with the XPS study of the Fe oxidation state of our sample. Similarly, For the $La_{0.7}K_{0.3}FeO_{3-\delta}$ sample, Fe^{4+}/Fe^{3+} oxidation states were found in the ratio of 54:46, and oxygen content was found to be 2.97.

6.3.3 Brunauer-Emmett-Teller (BET) analysis

N_2 adsorption-desorption isotherms with pore size distribution are shown for $LaFeO_3$ and $La_{0.5}K_{0.5}FeO_{3-\delta}$ is shown in **Figure 6.3** Surface area for pure $LaFeO_3$ was found to be 19m^2/g, and for $La_{0.5}K_{0.5}FeO_{3-\delta}$ sample it was 26 m^2/g. Both samples show a large number of pores with pore-size distribution between 2nm to 12nm in diameter.

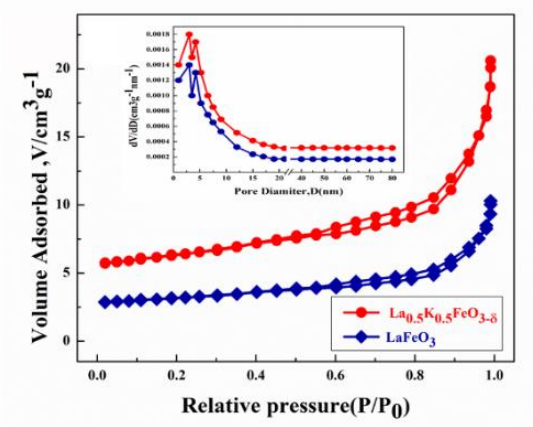

Figure 6.3 show N_2 adsorption-desorption isotherms with the pore size distribution

6.3.4 Scanning Electron Microscopy (SEM) with Analysis (EDX) and High-Resolution Transmission Electron Microscopes (HRTEM) analysis

SEM image is shown in **figure 6.4.(a)** presents the porous sphere type particle morphology of the $La_{0.5}K_{0.5}FeO_{3-\delta}$ sample. Particle size distribution was calculated by **ImageJ** software. Particle size distribution was fitted with Gaussian distribution, and particle diameters were found in the range of 0.856μm to 1.38μm with an average particle diameter of about 1.3μm. **Figure 6.4.b** show HRTEM images of the sample. Lattice fringes are visible in the inverse Fast Fourier transform (FFT) (mapping with Gatan Digital micrograph software) of this region, confirming the crystalline nature of $La_{0.5}K_{0.5}FeO_{3-\delta}$. Lattice fringe spacing is in agreement with interplanar spacing obtained from XRD results.

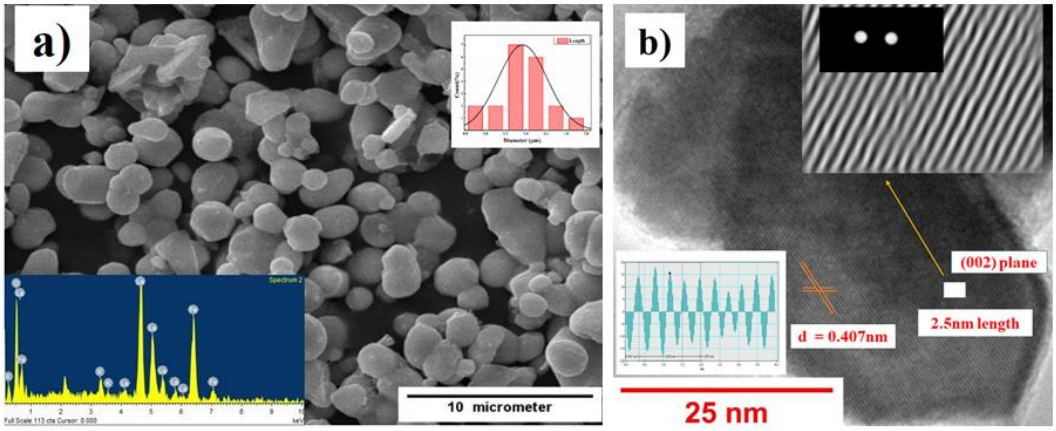

Figure 6. 4. (a) SEM image showing morphology characteristic of $La_{0.5}K_{0.5}FeO_{3-\delta}$ and particles distribution from SEM image, (b) HRTEM image comprising the plane with

distorted fringes (inset: FFT and inverse FFT of the selected region) of (002) plane and line profile of (002) plane the selected line in the inverse FFT image of the superstructural peak region.

6.3.5 Cyclic Voltammetry analysis

Electrochemical performance of $La_{1-x}K_xFeO_{3-\delta}$ ($0 \leq x \leq 0.5$), samples were determined using from cyclic voltammetry and galvanostatic charge/discharge curve. All sample of $La_{1-x}K_xFeO_{3-\delta}$ ($0 \leq x \leq 0.5$), were studied in 2M KOH electrolyte in the voltage range of 0 to -1V. We did perform the study up to -1V because below that we observed oxygen reduction reaction (ORR) over our electrode and this creates a loss of capacitance of the materials. **Figure 6.5 (a)** represents the comparative cyclic voltammetry curve for $La_{1-x}K_xFeO_{3-}$($0 \leq x \leq 0.5$), with increasing K concentration, $Fe^{4+/3+}$ and $Fe^{3+/2+}$ redox peak appear shifted to lower potential linearly. For example in undoped $LaFeO_3$, $Fe^{3+/2+}$ redox couple appear at -0.84V, in $La_{0.7}K_{0.3}FeO_{3-\delta}$ it was appear at -0.64V and in $La_{0.5}K_{0.5}FeO_{3-\delta}$ it appear at -0.59V. Similarly $Fe^{4+/3+}$ couple appear at -0.85V in $La_{0.5}K_{0.5}FeO_{3-\delta}$ and at -0. 89 V in $La_{0.7}K_{0.3}FeO_{3-\delta}$ and did not appear up to -1V for undoped $LaFeO_3$. Thus the inductive internal potential arises due alternation of the La and K layer over Fe-O octahedra (as shown in **Figure. 6.1 (c)** made $Fe^{4+/3+}$ redox couple accessible for electrochemical performances. Cyclic Voltammetry curve for $La_{1-x}K_xFeO_{3-\delta}$ (x = 0, 0.3, 0.4, 0.5) with different scan rates are shown in **Figure 6.5 (b-d)** respectively. For x = 0.3 composition, $La_{0.7}K_{0.3}Fe_{0.55}^{4+}Fe_{0.46}^{3+}O_{2.97}$, with an almost equal concentration of Fe^{4+} and Fe^{3+} state, both $Fe^{4+/3+}$ and $Fe^{3+/2+}$ redox peak seem to operate in a very close voltage range representing a clean diffusion-controlled behaviour of the electrode. However, a low capacity output has resulted for the $La_{0.7}K_{0.3}Fe_{0.55}^{4+}Fe_{0.46}^{3+}O_{2.97}$electrode. The quasi rectangular shape of the curve suggests the dominance of pseudo-capacitance behaviour over EDLC. The specific capacitance C (F/g) was calculated to understand the electrochemical performance of the working electrode as represented by **equation 6. 1**.

$$Csp = \frac{\int I\,(V)dV}{mV\nu} \qquad (6.1)$$

Where I (A) is the cathodic current, ν ($V \cdot s^{-1}$) is the scan rate, m (g) is the mass of active material, and V (V) is the sweep potential window. [35]

Gravimetric capacitance of $La_{1-x}K_xFeO_{3-\delta}(0 \leq x \leq 0.5)$, materials from Cyclic Voltammetry curve at scan rate of 1mV/s was found to be 95F/g, 113F/g, 143F/g, 203F/g, 394F/g and 662F/g respectively. The capacitance of $La_{0.5}K_{0.5}FeO_{2.92}$ which contains almost 84% Fe in the Fe^{4+} oxidation state confirmed by XPS and iodometry titration study was found to be ~662 F/g suggesting more than one electron or anion transfer per molecule. In an aqueous KOH electrolyte with predominant OH^- transportation, the redox reaction pseudo-capacitive storage can be represented as

$$La_{1-x}K_x[Fe^{4+}Fe^{3+}]O_{3-\delta} + 2ye^- + yH_2O \leftrightarrow La_{1-x}K_x[Fe^{3+/2+}]O_{3-y-\delta}[OH^-]_{2y} \quad (6.2)$$

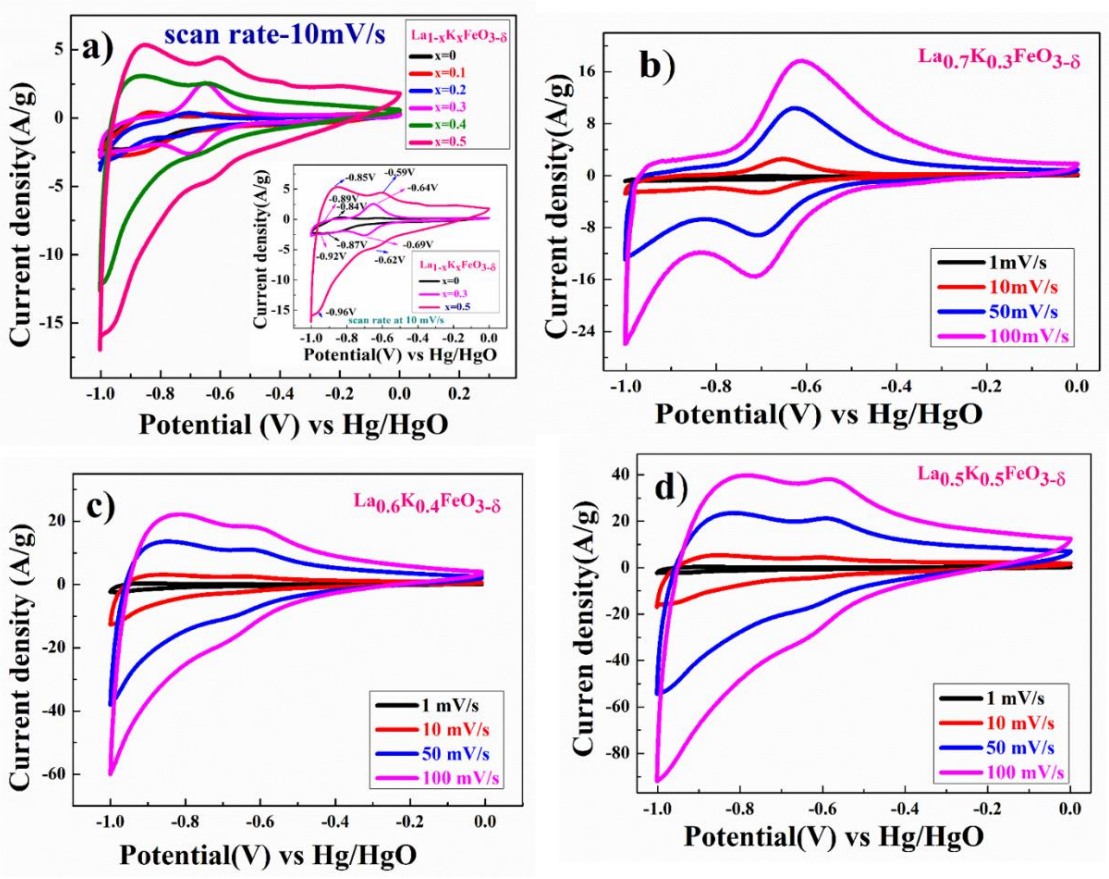

Figure 6.5 (a) Cyclic voltammetry of $La_{1-x}K_xFeO_{3-\delta}$ ($(0 \leq x \leq 0.5)$,) material at scan rate 10 mV/s in 2M KOH electrolyte, (b-d) cyclic voltammetry of $La_{1-x}K_xFeO_{3-\delta}$ (x = 0.3, 0.4, 0.5) material in 2M KOH electrolyte

Thus the formation of $La_{1-x}K_x[Fe^{3+/2+}]O_{3-y-\delta}[OH^-]_{2y}$ is resulting pseudo-capacitance through OH^- intercalation coupled with surface adsorption. For y = 0.5, with

intercalation of one OH^- coupled with $1e^-$ charge transfer, the theoretical capacity of **$La_{0.5}K_{0.5}FeO_{2.92}$** should be ~500 F/g, and therefore with the observation of ~662 F/g capacity of the electrode, the equivalent charge transfer of 1.32 e^- or OH^-/H_2O transport/transfer taken place per molecule of $La_{0.5}K_{0.5}FeO_{2.92}$.

Thus for $La_{0.5}K_{0.5}[Fe^{4+}_{0.84;}\ Fe^{3+}_{0.16}]\ O_{2.92}$, redox reaction can be represented as

$$La_{0.5}K_{0.5}\ [Fe^{4+}_{0.84}Fe^{3+}_{0.16}]\ O2.92 + 1.32e^- + 0.66H_2O \leftrightarrow La_{0.5}K_{0.5}[Fe^{3+}_{0.72}Fe^{+2}_{0.28}]O_{2.36}[OH^-]_{1.32} \quad (6.3)$$

6.3.6 Determination of the Diffusion coefficient

To understand the electrochemical kinetics of the $La_{1-x}K_xFeO_{3-\delta}$ (x = 0, 0.3, 0.5) sample, the plot of anodic and cathodic peak current concerning the square root of scan rate is plotted in **Figure 4. (e)**. Linear fitting of these plots represents the semi-infinite diffusion-controlled process. The kinetics of electrodes can be examined with the help of the diffusion coefficient. Determination of the diffusion coefficient of those electrodes was followed by using Randles-Sevick eq. [36]

$$i_p = 2.686 \times 10^5 \times n^{3/2}\, A\, D^{1/2}\, C_o v^{1/2} \quad (6.4)$$

Where i_p is peak current (A), n is the number of electrons transferred in the redox event (usually 1), A is electrode area in cm^2, D is diffusion coefficient in cm^2/s, C_o is OH^- ion concentration in mol/cm^3, v is scan rate in V/s.

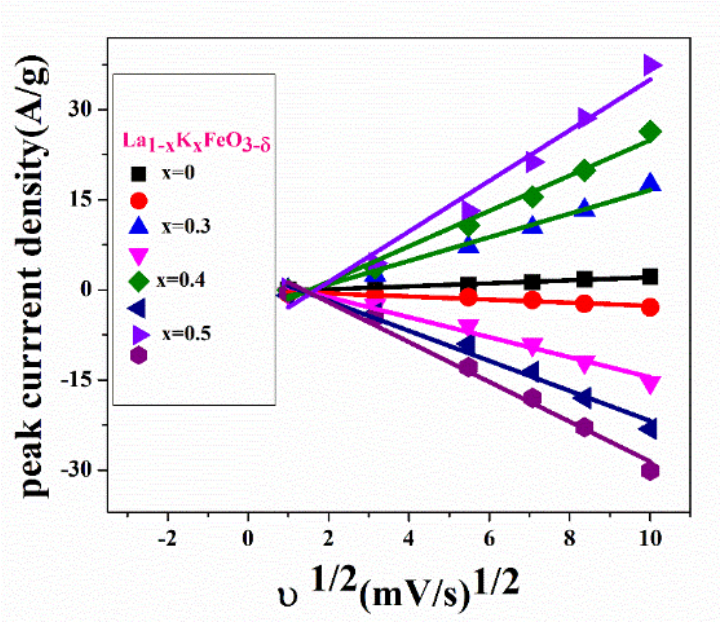

Figure 6.6 Plot peak current density vs square root of scan rate of $La_{1-x}K_xFeO_{3-\delta}$ (x = 0, 0.3, 0.5) sample

OH^- diffusion coefficient calculated using **equation (4)** at 1mV/s are presented in **table 6.2** For $La_{1-x}K_xFeO_{3-\delta}$ (x=0, 0.3, 0.4, 0.5) anode materials, forward reaction is charging and backward reaction discharging process. During the charging process, H_2O and e- react at the electrode surface to OH^- that is diffused through the surface to the lattice.[37] During discharge H_2O is exchanged through the lattice resulting in the recreation of the initial structure. Oxygen anion diffusion rates of PrBaCo2O6-δ (PBC) double perovskite with values of 14.7×10^{-12}, 1.8×10^{-12} and 0.3×10^{-12} cm^2 s^{-1} observed for measurements conducted in 9 M KOH, 1 M KOH and 0.1 M KOH electrolyte solutions[38]

Table 6.2: Determination of diffusion coefficient

Sample	Diffusion coefficient of anodic peak current(D_a) (cm^2/s)	Diffusion coefficient of cathodic peak current (D_c) (cm^2/s)
$LaFeO_3$	5.827×10^{-8}	5.998×10^{-8}
$La_{0.7}K_{0.3}FeO_{3-\delta}$	4.554×10^{-7}	3.889×10^{-7}
$La_{0.5}K_{0.5}FeO_{3-\delta}$	9.806×10^{-7}	7.711×10^{-7}

6.3.7 Determination of b values and analysis

The area under the curve from the CV plot represents the total charge stored through faradic and non-faradic reactions that occurred on the electrode surface. The current behaviour is generally followed by a power law and it is related to scan rate by the following equation;

$$i = av^b \qquad (6.5)$$

Where *a* and *b* are the variables that govern the nature of intercalation, *i* is the current (A), and ϑ is the scan rate (V/s). The value of b lies between 0.5 to 1, b = 0.5 stands for the diffusion control reaction or battery type behaviour, and b = 1 stands for the diffusion control faradic process involving charge transfer with surface/subsurface atoms. [39]

The b values for the $La_{0.5}K_{0.5}FeO_{3-\delta}$ sample were found to be varying linearly with the scan rates at different potentials ranging from -0.2 to -0.8V as shown in **Figure 6.7 (a-b)**. As shown in **Figure 6.7 (c),** in the charging process of anode material at -0.4V,

the b value was found to be 0.57 suggesting the dominance of the diffusion control process and except at -0.4V, on other potentials, the b values were found to be above 0.8 suggesting faradic process dominating surface couples redox-mediated capacitance behaviour. Similarly in discharging process, b values were found to be higher than 0.85 suggesting a redox pseudocapacitive process from charge transfer with surface/subsurface atoms.

The b values for $La_{0.5}K_{0.5}FeO_{3-\delta}$ electrode varied differently in two different regions; (1) below ≤10 mV/s and (2) ≥10 mV//s in Plot of log (peak current (A)) vs log (scan rate (mV/s)) as shown in **figure 6.7 (d)**. The b value for cathodic and anodic diffusion are 1 and 0.98 respectively below 10 mV/s, suggesting rapid surface control kinetic and the b value for cathodic and anodic diffusion are 0.87 and 0.7 above 10 mV//s suggesting a resistance at a high scan rate

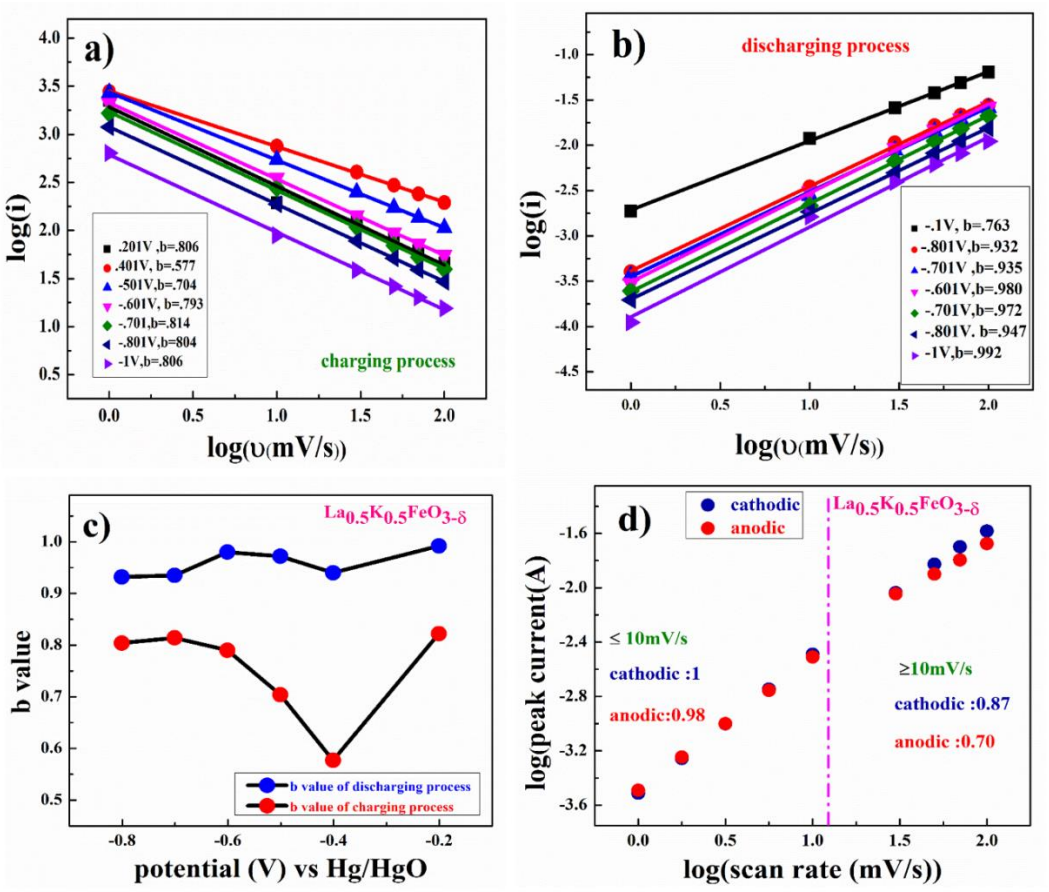

Figure 6.7 (a-b) shows the linear relationship of log (υ) vs log (i), slope represents the b value according to the power-law (c) b value at the different potential of $La_{0.5}K_{.5}FeO_{3-\delta}$ in charging and discharging process at a different potential, (d) plot of log(peak current) vs log(scan rate)

6.3.8 Dunn's plot analysis

Similarly, the Voltammetry sweep rate dependence on the current response can distinguish the capacitive contribution to the current response quantitatively by Dunn's methodology. The current response at a fixed potential is envisaged as the combination of two separate mechanisms, surface capacitive effects, and diffusion-controlled insertion. [40-41]

$$i(\upsilon) = K_1 v + K_2 v^{\frac{1}{2}} \quad (6.6)$$

For more understanding **eq.(6)** rearrange

$$\frac{i(\upsilon)}{\upsilon^{\frac{1}{2}}} = \frac{K_1}{\upsilon^{\frac{1}{2}}} + K_2 \quad (6.7)$$

K_1 υ and K_2 $\upsilon^{1/2}$ represent the current contributions from the surface capacitive effects and the diffusion-controlled intercalation process, respectively. Thus after the determination of k_1 and k_2, we can quantify the fraction of the current due to each of these contributions at specific potentials. With the linear fitting of **i(υ)/ $\upsilon^{1/2}$** vs **1/$\upsilon^{1/2}$** plot with different scan rates for the $La_{0.5}K_{0.5}FeO_{3-\delta}$ sample, k_1 and k_2 values are determined from the slope and intercept of the y-axis respectively. The representative curve of $i(\upsilon)/\upsilon^{1/2}$ vs. $\upsilon^{1/2}$ for the $La_{0.5}K_{0.5}FeO_{3-\delta}$ sample is shown in **Figure 6.8 (a, b).** Contribution of surface capacitance (69.62%) and diffusion controlled interaction (30.38%) was found for $La_{0.5}K_{0.5}FeO_{3-\delta}$ electrode at operating potential -0.6V with scan rate10mV/s as shown in **Figure 6.8 (c)**. Surface capacitance and diffusion-controlled interaction participations are varied linearly with varying scan rates. Surface capacitive and diffusion control contributions are 42%, 58% respectively at -0.6V with scan rate 1mV/s. Surface capacitive contribution increases with increasing scan rate; i.e., surface capacitive contribution and diffusion control contribution were found to be 88% and 12% respectively at 100 mV/s in **Figure 6.8 (d)**

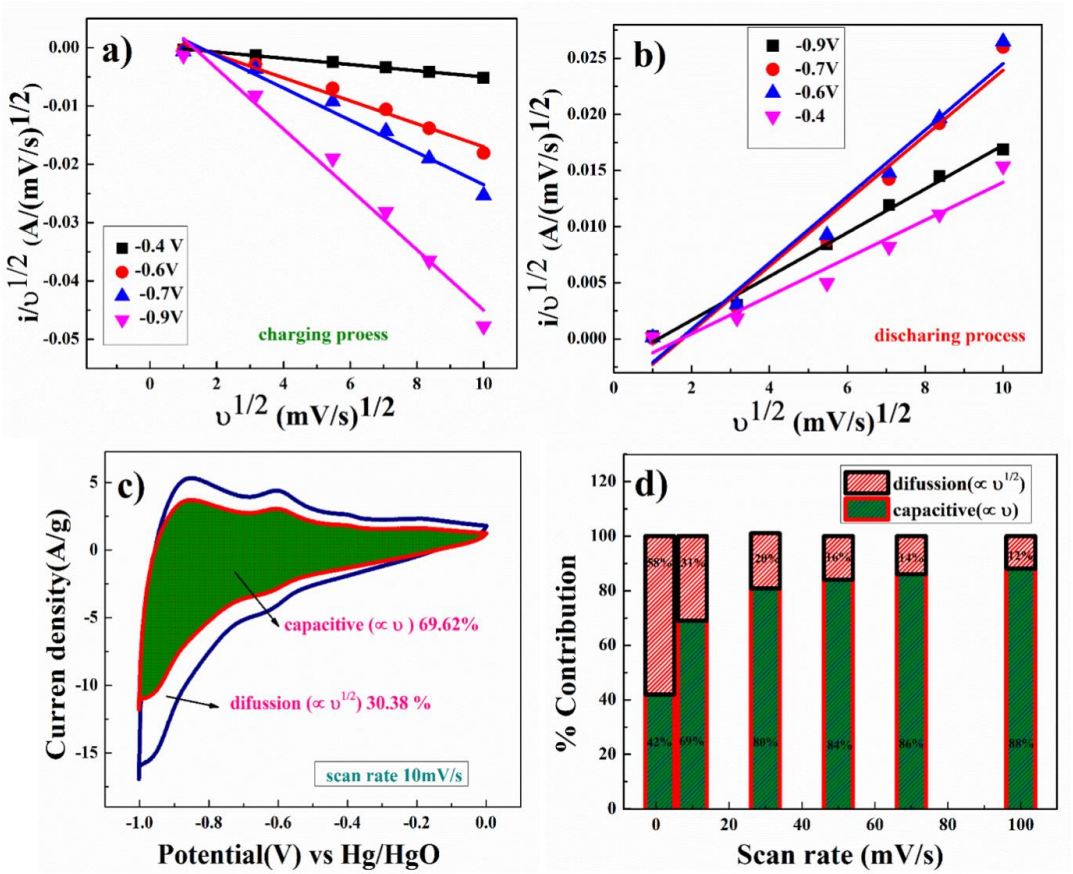

Figure 6.8 (a-b) capacitive and diffusion control processes contribution can be distinguished by the slope (k_1) and intercept (k_2) (c) capacitive and diffusion control process of $La_{0.5}K_{.5}FeO_{3-\delta}$ electrode at 10mV/s, (d) capacitive and diffusion control percentage with different scan rate at discharge peak potential (-0.96V)

6.3.9 Trassati's plot analysis

According to Trassati, the total specific capacitance is the sum of the intercalative (inner) and outer surface capacitance of the electrode. It can be expressed as

$$C_{total} = C_{in} + C_{out} \tag{6.8}$$

The specific capacitance contributed from the inner and outer surface of the electrode is dependent upon the scan rate. **Figure 6.9(a),** the y-intercept of the linear fit of 1/q vs. $\upsilon^{1/2}$ plot at υ=0, represents the total amount of charge stored in the electrode

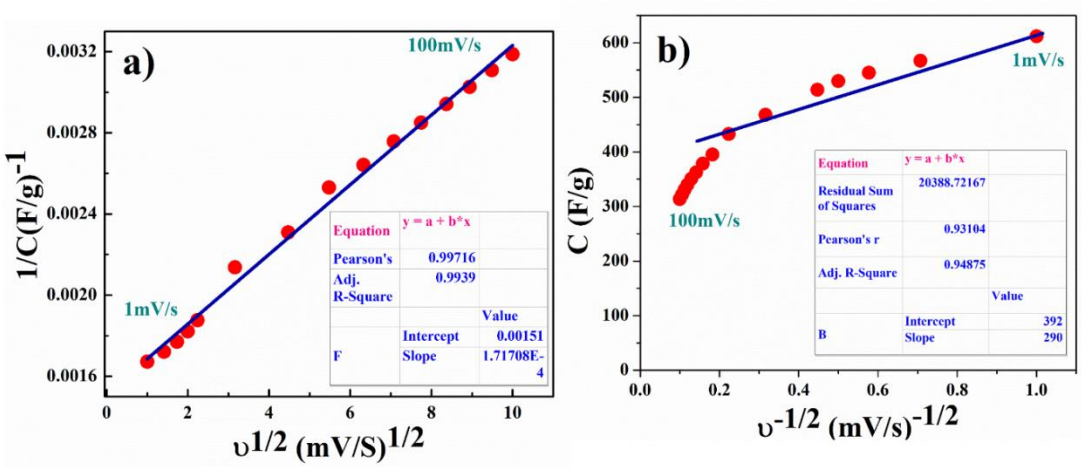

Figure 6.9 (a-b) corresponds to Trasatti plot at scan rate of 100mV/s to 1mV/s

In **Figure 6.9(b),** the y-intercept of the linear fit q vs. $\upsilon^{-1/2}$ plot $\upsilon = \infty$ corresponds to the amount of charge stored at the outer surface of the electrode. [42]. Applying Trassati plot outcome, it can be concluded that the total Capacitance value (C_{total} = 662 F/g) of $La_{0.5}K_{0.5}FeO_{3-\delta}$ was having intercalative inner surface contribution (C_{in}) equivalent to 359 F/g and outer surface contribution (C_{out}) was equivalent to 303 F/g.

6.3.10 Chonopotentiometry (charge-discharge)

Charge discharge measurement (Potential (V) vs. time (t)) was carried out at constant current by Chonoamperometry. The gravimetric capacitance value was calculated from the Potential (V) vs. time (t) plot by using the following equation given below,

$$C = \frac{I\triangle t}{mV} \qquad (6.9)$$

Where I (A) is the applying constant current, Δt (s) is the discharge time, m (g) is active mass, and V represents the operating potation window.[43]

The gravimetric capacitance of $La_{1-x}K_xFeO_{3-\delta}$ ($0 \leq x \leq 0.5$), electrode from the charge-discharge plot is shown in **Figure 6.10 (a)** and at the current rate of 1A/g their values were found to be 101 F/g, 117 F/g, 148 F/g 226 F/g, 389 F/g and 619 F/g respectively. Gravimetric capacitance values in **Figure 6.10 (b)** are found to 619 F/g, 347 F/g, 188 F/g, 121 F/g, 65 F/g respectively at constant current of 1 A/g, 2 A/g, 3 A/g, 5 A/g, 10 A/g for $La_{0.5}K_{0.5}FeO_{3-\delta}$ electrode. Capacitance performance with different cycle numbers of $La_{0.5}K_{0.5}FeO_{3-\delta}$ electrode is shown in **Figure 6.10 (c)**. Up to 88.5% capacitive retention and columbic efficacy (95%) were obtained for

continuous 5000 cycles of charge/discharge for $La_{0.5}K_{0.5}FeO_{3-\delta}$ electrode at 5A/g constant current as shown in **Figure 6.10 (d)**.

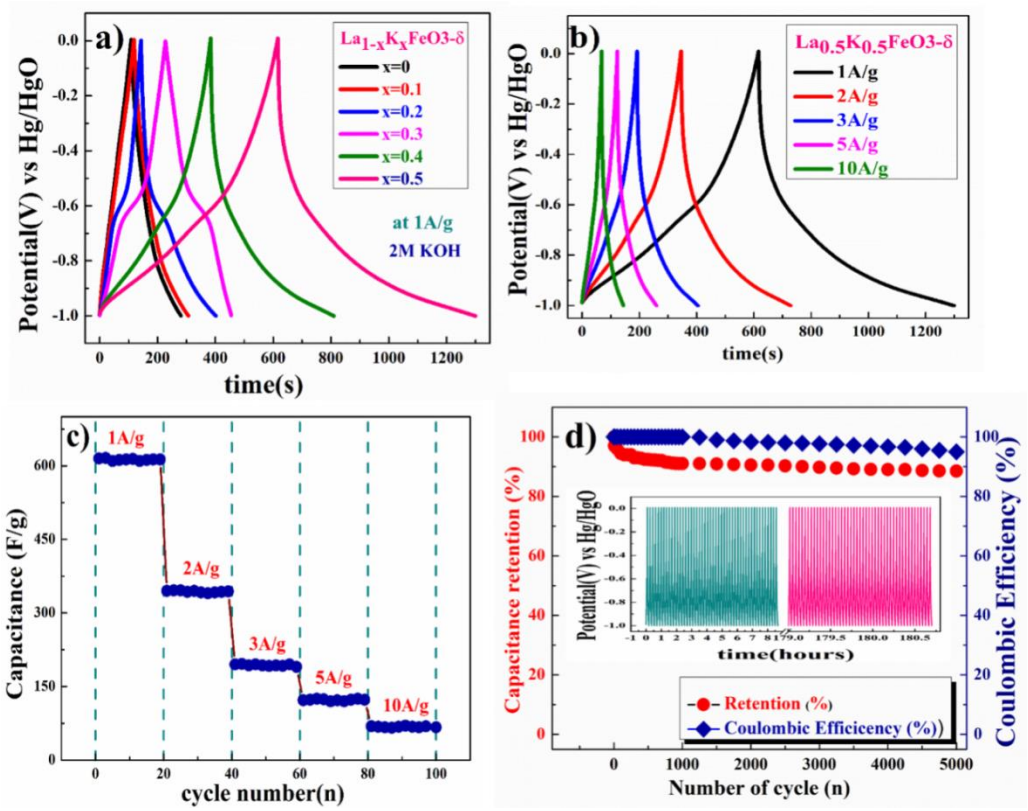

Figure 6.10 a) Charge−discharge plot (V vs time) of the $La_{1-x}K_xFeO_{3-\delta}$ ($0 \leq x \leq 0.5$), electrode at 1 A/g; (b) charge−discharge plot (potential (V) vs time (t)) of the $La_{0.5}K_{0.5}FeO_{3-\delta}$ electrode; (c) capacitance performance of the $La_{0.5}K_{0.5}FeO_{3-\delta}$ in 2 M KOH electrolyte at different constant currents; (d) capacitive retention and Coulombic efficiencywith cycle number.

6.3.11 Electrochemical impedance spectroscopy (EIS) analysis

Electrochemical impedance spectroscopy (EIS) measurement was carried out at AC voltage at 10mV applied voltage from 1 MHz to 0.01 Hz range and shown by Nyquist plot in **Figure 6.11** for $La_{1-x}K_xFeO_{3-\delta}$ (x = 0, 0.3, 0.4, 0.5) electrodes. The specific impedance contribution is mainly attributed to the impedance distributions over electric series resistance (Rs), charge transfer resistance (Rct), and Warburg impedance (Rw).

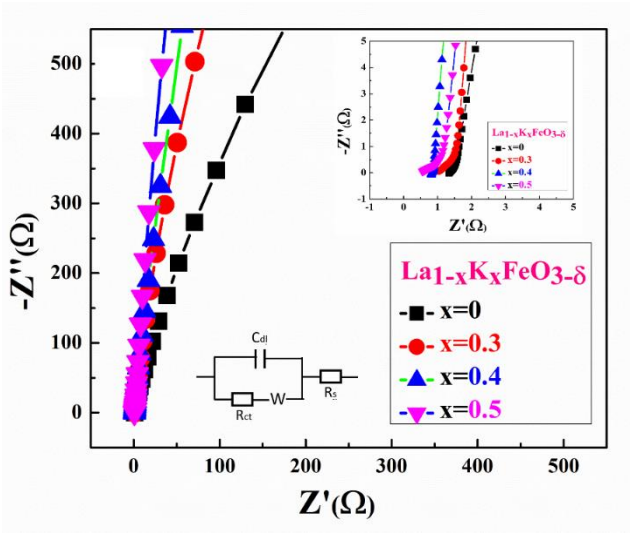

Figure 6.11 Electrochemical impedance spectroscopy (EIS) at 10 mV applied voltage from 1 MHz to 0.1 Hz.

Higher frequency resistance $La_{1-x}K_xFeO_{3-\delta}$ electrode gradually decreases with increasing K ion substitution in the sample as electronic conductivities of the samples were increasing with increasing K doping. Lower frequency data represent the Warburg diffusion resistance and for La_{1-x} $K_xFeO_{3-\delta}$ (x = 0, 0.3, 0.4, 0.5) samples the straight line in the low-frequency region is close to 90° angle (very close to –Z″(Ω) axis) from horizontal line represents the characteristic of pseudo capacitance behaviour of $\mathbf{La_{0.5}K_{0.5}FeO_{3-\delta}}$ electrode. This also represents fast OH^- ion diffusion in the porous structure**.**

6.3.12 Two electrodes full cell test of $La_{0.5}K_{0.5}FeO_{3-\delta}$ //AC (CV, charge-discharge, and cyclic stability)

To understand the real charge storage behaviour of $La_{0.5}K_{0.5}FeO_{3-\delta}$ relative to AC (Activated carbon), two electrode ASCs (Asymmetry Supercapacitors) measurements have been conducted in 2 M KOH. To determine the maximum specific capacitance during the full test, the storage capacity of positive and negative electrodes need to be balanced as per the following equation:

$$\frac{1}{C_{total}} = \frac{1}{C_{positive}} + \frac{1}{C_{negative}} \qquad (6.10)$$

For balancing the charge storage capacity of the cell, the mass ratio (m^+/m^-) of positive and negative electrode material was measured using the following equation:

$$\frac{m^+}{m^-} = \frac{C_- \times \Delta E_-}{C_+ \times \Delta E_+} \qquad (6.11)$$

$m^+, m^-, C_+, C_-, \Delta E_+, \Delta E_-$ are mass, specific capacitance, and potential window of positive and negative electrodes estimated by three-electrode measurement.[36-37]

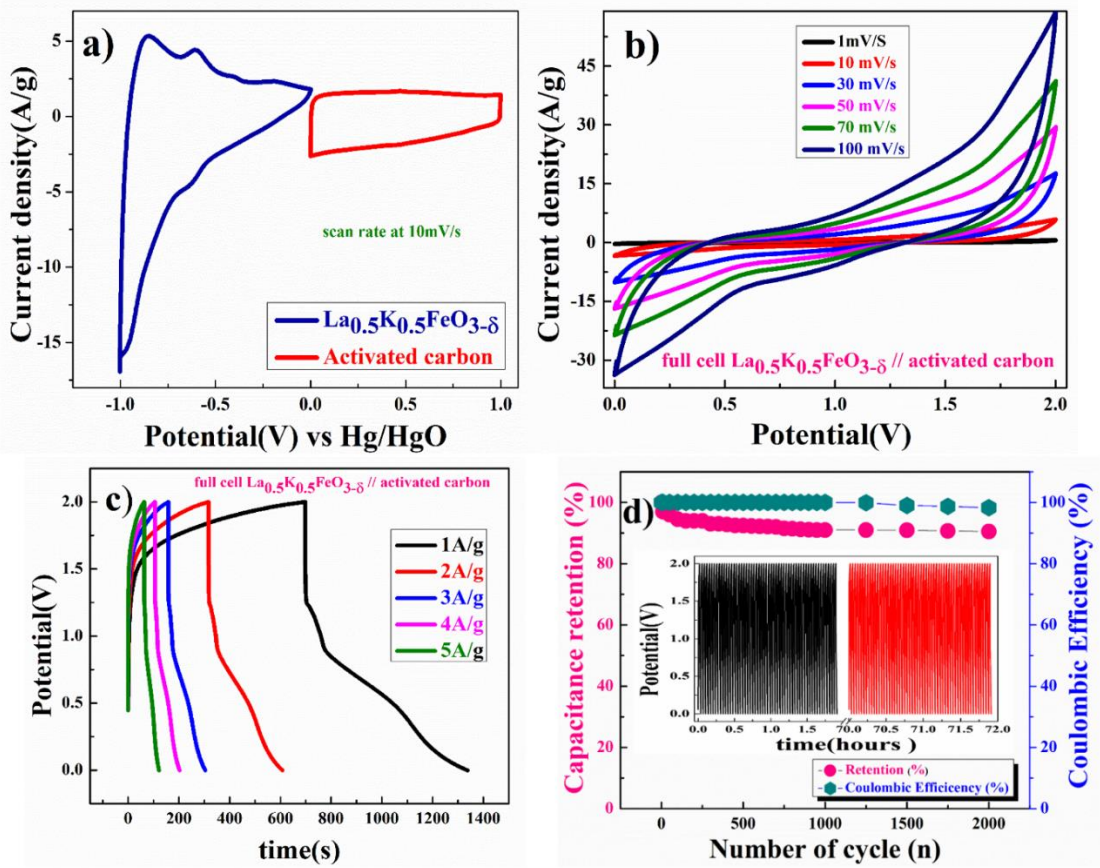

Figure 6.12 Full-cell (ASC) performances of activated carbon vs the $La_{0.5}K_{0.5}FeO_{3-\delta}$ electrode. (a) CV of individual electrodes at 10 mV/s concerning the Hg/HgO electrode; (b) CV at different scan rates of ASCs; (c) charge−discharge plot; (d) capacitance retention and Coulombic efficiency with 2000 cycles at 5 A/g constant currents of the full cell

Figure 6.12 a) shows CV at a 10 mV/s scan rate where used AC (activate carbon) act as the positive electrode and $La_{0.5}K_{0.5}FeO_{3-\delta}$ act as the negative electrode. The calculated mass ratio ($\frac{m^+}{m^-}$) was found 1: 2.23 for the asymmetric cell and the weight of the active materials was taken to be 3.3 mg (excluding the weight of acetylene black and PVDF). **Figure 6.12.b)** demonstrate the CV curve of $La_{0.5}K_{0.5}FeO_{3-\delta}$ //AC two electrodes in ASCs mode at different scan rates, ranging from 1 mV/s to 100 mV/s in potential window 2 V to access the possible change the oxidation states are

Fe from Fe^{2+} to Fe^{4+}. **Figure 6.12 C)** subsequently, shows the charge/discharge curve conducted for measuring the capacitance of the electrode, capacitance values were calculated by **equation 9**. Capacitances for $La_{0.5}K_{0.5}FeO_{3-\delta}$ electrodes were found to be 348 F/g, 290 F/g, 228 F/g, and 147 F/g at current densities of 1 A/g, 2 A/g, 3 A/g, and 5 A/g respectively. **Figure 6.12.e)** show that the Coulombic efficiency of two electrode full cell has lost only 3% with higher capacity retention close to 90.5% of its initial value after 2000 cycles at constant current equivalent to 10 A/g.

6.3.13 Electrochemical impedance spectroscopy (EIS) of two electrode ($La_{0.5}K_{0.5}FeO_{3-\delta}$//AC full cell)

Figure 6.13 show the EIS plot (Nyquist) in the frequency range (1MHz to 0.1Hz) at 10 mV applied voltage) confirming superior charge transfer and higher capacitance of $La_{0.5}K_{0.5}FeO_{3-\delta}$//AC) in full cell mode.

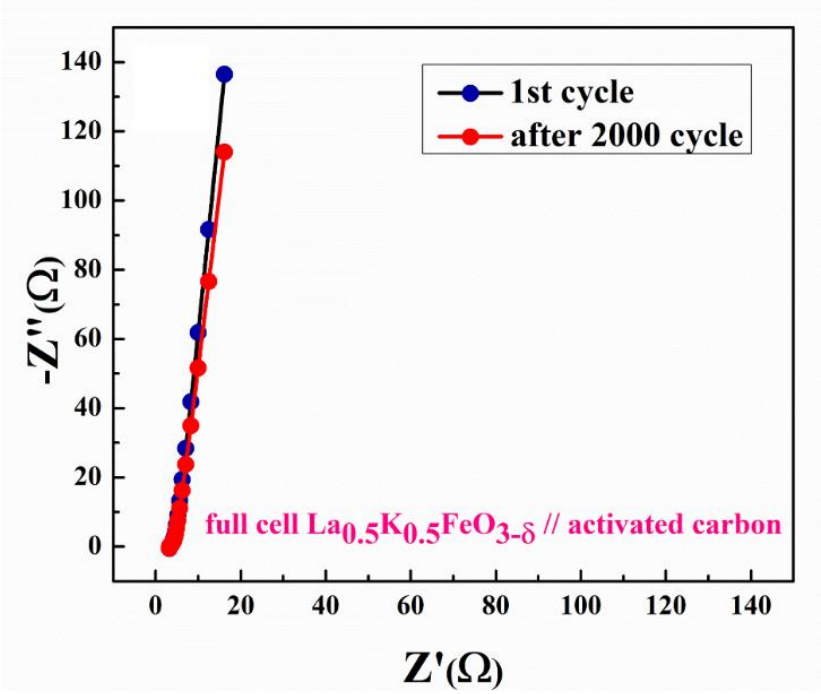

Figure 6.13 electrochemical impedance spectroscopy (EIS) at 10 mV applied voltage from 1 MHz to 0.1 Hz.

6.3.14 Study of specific energy Vs specific power of full cell ($La_{0.5}K_{0.5}FeO_{3-\delta}$//AC full cell)

Specific energy and specific power of asymmetric capacitors were calculated using the following equations.

$$E(Wh/kg) = \frac{1}{2}\frac{C_{ASCs}}{3.6}V^2 \quad (6.12)$$

$$P(W/kg) = \frac{E*3600}{t_{dis}} \quad (6.13)$$

Where C_{ASCs} is specific capacitance, V is operating voltage and t_{dis} is discharge time. [37]

Figure 6.14 shows the plot of specific energy vs specific power with different constant current rates. Resultant values show the highest specific energy equivalent to 193 Wh/kg at 1 A/g current density and specific power of ~1004 W/kg. Maximum specific power equivalent to ~3594 W/kg was obtained when specific energy was reduced to ~117 Wh/kg at 5 A/g of current density.

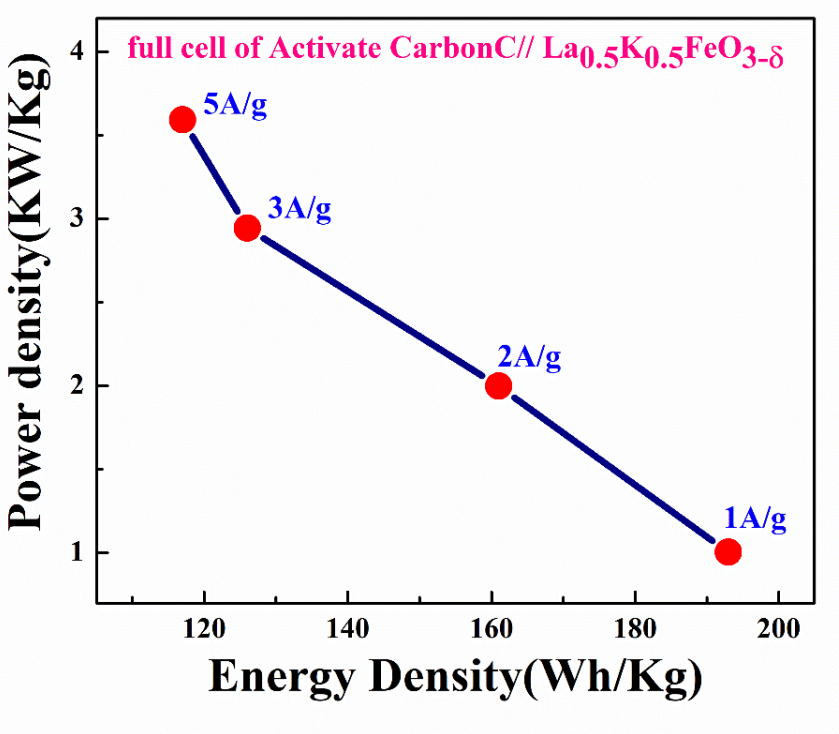

Figure 6.14 Ragone plot of the ASCs ($La_{0.5}K_{0.5}FeO_{3-\delta}$//AC) in full cell

6.4 Conclusions

In summary, it can be concluded that using induced inter-layer potential by altering La^{3+} and K^{+} layer in $La_{1-x}K_xFeO_{3-\delta}$, $Fe^{4+/3+,}$ and $Fe^{3+/2+}$ redox energies can be tuned and made accessible to envisage higher capacity (662 F/g equivalents to 1.32 e^-/OH^- diffusion) for $La_{0.5}K_{0.5}FeO_{2.92}$ electrode. Higher b values (>0.8) obtained for diffusion-controlled reaction suggest a high faradaic pseudocapacitive contribution to the electrode. With Trassati plot also, higher degree of inner layer contribution 54% (C_{in} = 359 F/g) to the total Capacitance (C_{total} = 662 F/g) was obtained for $La_{0.5}K_{0.5}FeO_{3-\delta}$ electrode. Up to 88.6% capacitive retention and coulombic efficiency (95%) were obtained after continuous 5000 cycles of charge/discharge and Maximum specific power of ~3594 W/kg was obtained when specific energy reached ~117 Wh/kg at 5A/g of current density for $La_{0.5}K_{0.5}FeO_{3-\delta}$ electrode in two-electrode $La_{0.5}K_{0.5}FeO_{3-\delta}$ //AC full cell mode with the remarkable stability of the electrode making the $La_{0.5}K_{0.5}FeO_{3-\delta}$ electrode suitable as a negative electrode for pseudo-capacitor applications.